AIAA SciTech Forum
6-10 January 2020, Orlando, FL
AIAA Scitech 2020 Forum

10.2514/6.2020-0555

Aeroelastic encounters of spanwise vortex gusts and the self-rotation of trailing vortices

Huansheng Chen* and Justin W. Jaworski †
Lehigh University, Bethlehem, Pennsylvania, 18015

Vortex structures in the atmosphere and in the wakes of aircraft generate fluid loads that may be beneficial (e.g., a reduction of induced drag) or detrimental (e.g., cause unsteady buffeting or dynamic instability) depending on the aerodynamic scenario at hand. Two distinct models are developed here to (i) investigate separately the aeroelastic effects of spanwise-oriented gusts encountering an airfoil and (ii) predict the self-rotation of a perturbed streamwise-oriented trailing vortex.

In Part I, the dynamically-coupled interactions of vortex gusts encountering a symmetric Joukowski airfoil on linear elastic supports is formulated analytically and evaluated numerically using a time-dependent conformal mapping technique. The Brown and Michael framework models the unsteady shedding of vorticity from the airfoil into the wake. Special attention is paid to the influence of the strength of the incident vortex and the airfoil natural frequency on the initial upstream placement of a vortex gust that achieves direct impingement on the airfoil. The results indicate a weak sensitivity of initial vortex position in the limits of a small or large structural natural frequency, while the initial vortex position changes monotonically with vortex strength. A comparison of the present numerical inviscid model to available experimental vortex gust measurements over stationary airfoils highlights the appropriate use of the point-vortex model for inviscid vortex-airfoil interaction problems without vortex strength decay, but also its inability of the model to model the dominant viscous interactions that occur for close vortex-airfoil encounters.

Part II employs the asymptotic analysis of a sinusoidally-deformed infinite vortex with a finite core to estimate the self-induced rotation of a trailing vortex produced by a wing tip. A comparison of the model against high-fidelity computational simulations indicates that the theory overpredicts the rotation rate, which generally depends on the amplitude of vortex deformation that is not present in the theoretical analysis.

I. Introduction

The encounter of a vortex gust with an aerodynamic body is a canonical fluid-structure interaction with implications for the prediction of transient loads on fliers and swimmers and their generation of vortex sound. Among the various orientations that the incident vortex can take with respect to the solid body (cf. Rockwell [1]), the alignment of the spanwise vortex with the orientation of the bound vorticity on the body, the wake, and the boundary-layer vorticity allows for their coupled interactions during a vortex-airfoil encounter. For this reason, a number of theoretical, numerical, and experimental studies have been carried out to understand and model two-dimensional vortex-structure interactions.

Dynamic stuctural motions affect the paths of the incident vortex and the unsteady vorticity shed into the wake, which thereby affect the unsteady fluid loading on the aerodynamic structure. These structural motions may be either prescribed or the result of aeroelastic coupling, where in the latter case the elasticity of the structure or its supports provides the route for two-way energy transfer between the solid and fluid. Early research carried out by Howe [2] involved a line vortex cut by a flat rigid plate under spring supports, which caused energy to be transferred from the turbulence to the restoring spring force. In a later contribution, Manela [3] studied the combined effects of a vortex converting past by an flexible sheet. These model problems focus only on a setup where the structure has unprompted motion under external loads, such as spring forces, but the fluid load and the effects of the structure motion on the turbulence are both ignored. Recently, Manela [4] considered the nonlinear effects of flow unsteadiness on a flat plate with periodic oscillation motions, which include the effects of the plate motion on the turbulence. However, existing studies have not considered the *coupled* effects of incident vorticity and structure under *aeroelastic* motion, which

*Ph.D. Student, Department of Mechanical and Mechanics, Student Member AIAA
†Assistant Professor, Department of Mechanical and Mechanics, Senior Member AIAA

motivates the present work. An investigation by Manela [4] also provides the verification case in the present work for the limit of zero airfoil thickness.

Apart from these studies of vortex-structure interactions listed above, special attention has been paid to the effects of structure configuration and vortex placement on direct vortex impingement. Early experiments performed by Rockwell and Knisely [5] investigated the impinging vortex motions excessively, later Ziada and Rockwell [6] observed a point vortex impinging upon the leading edge of a wedge. Other numerical modelling works of the associated flow physics in the vortex-structure interaction has been developed by Conlisk and Rockwell [7], Conlisk and Veley [8], and Panaras [9]. So far, analytical investigations of direct vortex impingement have not been developed for structures under aeroelastic motions and is a key contribution of the present study.

The present work is organized into two independent parts. The first part models the vortex-wake interactions for non-flat airfoil geometries, and the aeroelastic interactions with linear elastic mount. The model may be used to predict the conditions for direct vortex impingement. The model scenario and dynamic formulation are discussed in this paper has been studied previously by Chen and Jaworski [10]. This paper also contains comparison results of previous analytical and experimental study for simple setups of airfoil, and the investigation on the effects of vortical or structural parameters on vortex impingement. The second part starting in Section IV develops a simple model for the self-rotation of an infinite, finite-core vortex that is initially straight and is given a small-amplitude, sinusoidal deformation along its axis. The rotation rate from asymptotic analysis is compared against high-fidelity computations by Garmann and Visbal [11] for a Batchelor vortex emerging from an inflow boundary. The predicted and computed rotation rates are compared and contrasted with respect to the flow parameters and the different physical scenarios of the theoretical and computational setups.

Part I

II. Mathematical Formulation

Figure 1 illustrates the model problem of a Joukowski airfoil on elastic supports in two-dimensional uniform flow with an incident line vortex Γ and the vorticity field Σ shed into the wake. All vortices are defined to have positive circulation in the anticlockwise direction. The strength of the trailing-edge vortex γ_n satisfies the Kutta condition, and its motion obeys the emended Brown and Michael equation [12]. The mathematical formulation of the aeroelastic system is now described.

A. Mapping

The conformal mapping of the Joukowski airfoil between the physical z-plane and the mapped ζ-plane is described by

$$\zeta(z) = \frac{1}{2}\left(z + \sqrt{z^2 - 4\lambda^2}\right) - f_0. \tag{1}$$

Using Eq. (1), the Joukowski airfoil in the physical z-plane ($z = x + iy$) with its trailing edge locating at $(2\lambda, 0)$ is mapped to a circle with radius $r = 1$ in the f-plane ($f = f_1 + if_2$), as shown in Fig. 2. Note the offset of the circle center at $f_0 = f_{x0} + if_{y0}$ and the corresponding trailing edge at $(\lambda, 0)$. For the symmetric Joukowski airfoils considered in this work, $f_{y0} = 0$. The unit circle in the f-plane is then shifted by an elementary mapping to the origin in the ζ-plane.

When time-dependent airfoil motions are considered, Eq. (1) becomes

$$\zeta(s) = \frac{1}{2}\left[s(z,t) + \sqrt{s^2 - 4\lambda^2}\right] - f_0, \tag{2}$$

where $s(z,t) = z - ih(t)$. The airfoil displacement $h(t)$ may be either prescribed or be part of the solution, as in the case of aeroelastic airfoil motions.

B. Flow complex potential

The complex potential of the flow is

$$w(\zeta) = w_\gamma + w_\Gamma + w_h + U\left(\zeta + f_0 + \frac{\lambda^2}{\zeta + f_0}\right), \tag{3}$$

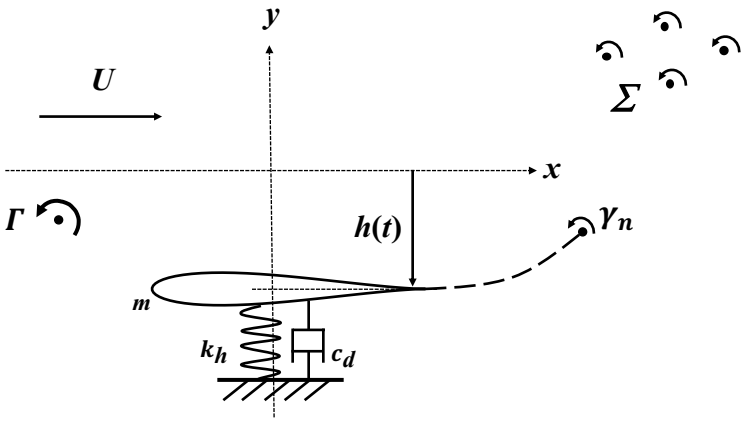

Fig. 1 Schematic of the generalized model problem of an incident vortex interaction with a symmetric Joukowski airfoil on elastic translational support in a uniform flow, where U is the flow speed and $h(t)$ denotes the displacement of the airfoil. The airfoil can be considered as a damped harmonic oscillator with mass m, damping coefficient c_d, and spring stiffness k_h. Γ denotes the incident line vortex, and γ_n is the tethered trailing-edge vortex whose motion is determined by the emended Brown and Michael equation. Σ is the set of free vortices generated at the airfoil trailing edge due to unsteady airfoil loads in response to the incident line vortex or the airfoil motion. The airfoil has zero angle of attack.

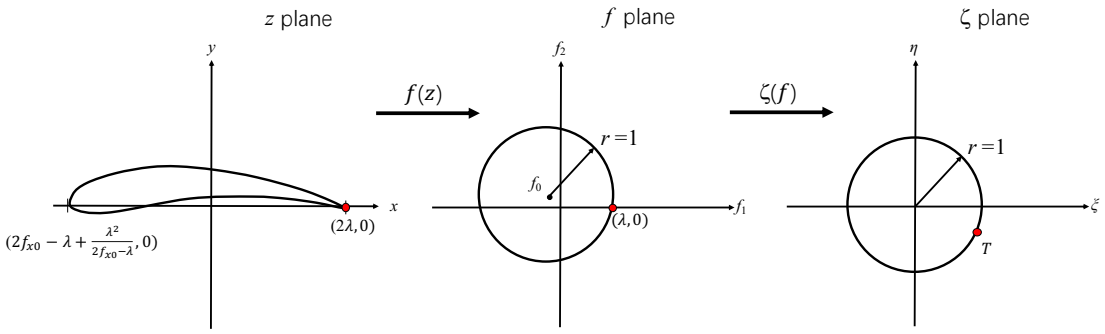

Fig. 2 Successive mappings of a generalized Joukowski airfoil in the physical z-plane to a unit circle centered at the origin in the ζ-plane, T is the trailing edge location.

where $w_\gamma(\zeta)$, $w_\Gamma(\zeta)$, and $w_h(\zeta)$ are the contributions due to the shed and free vorticity field, the incident vortex, and the airfoil motion, respectively. The last term of Eq. (3) represents the uniform background flow.

The complex potential of the incident vortex $w_\Gamma(\zeta)$ is determined from the model of a vortex moving around a cylinder [13], which yields,

$$w_\Gamma(\zeta) = -\frac{i\Gamma}{2\pi}\log\left(\zeta - \zeta_\Gamma\right) + \frac{i\Gamma}{2\pi}\log\left(\zeta - \frac{1}{\zeta_\Gamma^*}\right) - \frac{i\Gamma}{2\pi}\log\zeta, \tag{4}$$

where the last two terms guarantee that the total circulation inside the cylinder is initially zero, and the asterisk superscript denotes the complex conjugate. Similarly, the complex potential of the vortices shed into the wake is

$$w_\gamma(\zeta) = \sum_{k=1}^{n}\left(-\frac{i\gamma_k}{2\pi}\log\left(\zeta - \zeta_{\gamma_k}\right) + \frac{i\gamma_k}{2\pi}\log\left(\zeta - \frac{1}{\zeta_{\gamma_k}^*}\right)\right). \tag{5}$$

By appeal to Kelvin's theorem, the bound vorticity inside the cylinder at any time has total circulation $-\sum_{k=1}^{n}\gamma_k$, which is used to compute the aerodynamic lift force.

The complex potential of the airfoil motion is [14],

$$w_h(\zeta) = iV\left(\zeta - \frac{1}{\zeta}\right), \tag{6}$$

where $V = \mathrm{d}h/\mathrm{d}t$ is the instantaneous velocity of the airfoil in the downward direction.

C. Vortex shedding and the emended Brown and Michael equation

The motions of the shed vortices are described by the emended Brown and Michael equation [12],

$$\frac{\mathrm{d}\boldsymbol{x}_{\gamma_n}}{\mathrm{d}t}\cdot\boldsymbol{\nabla}\Psi_j + \frac{\Psi_j}{\gamma_n}\frac{\mathrm{d}\gamma_n}{\mathrm{d}t} = \boldsymbol{v}_{\gamma_n}\cdot\boldsymbol{\nabla}\Psi_j, \qquad j = 1, 2, \tag{7}$$

where $\boldsymbol{x}_{\gamma_n}$ represents the location of a shed vortex tethered to the trailing edge with circulation γ_n, and $\boldsymbol{v}_{\gamma_n}$ is the fluid velocity when the local velocity induced by γ_n is excluded. Here a Cartesian coordinate system is considered, where $\boldsymbol{x} \equiv (x, y)$. $\Psi_j(\boldsymbol{x}, t)$ denotes the stream function of the complex potential of the flow in the j-direction. For a Joukowski airfoil mapped to the ζ-plane, the components of the stream function are [15]

$$\Psi_1 = \mathrm{Im}\left\{\zeta + \frac{1}{\zeta}\right\} \quad \text{and} \quad \Psi_2 = \mathrm{Im}\left\{-i\left(\zeta - \frac{1}{\zeta}\right)\right\}. \tag{8}$$

The instantaneous circulation of the tethered vortex $\gamma_n(t)$ is obtained by enforcing the Kutta condition at the trailing edge of each instant in time,

$$\gamma_n(t) = \frac{\left|T^*\zeta_{\gamma_n} - 1\right|^2}{\left|\zeta_{\gamma_n}\right|^2 - 1}\left(\frac{2\Gamma\left(1 - \mathrm{Re}\{T^*\zeta_\Gamma\}\right)}{\left|T^*\zeta_\Gamma - 1\right|^2} - \sum_{k=1}^{n-1}\gamma_k\frac{\left|\zeta_{\gamma_k}\right|^2 - 1}{\left|T^*\zeta_{\gamma_k} - 1\right|^2} - 2\pi V\,\mathrm{Re}\{T^*\}\right), \tag{9}$$

in which T^* is complex conjugate of the trailing edge T location ($T = \lambda - f_0$) in the ζ-plane. The tethered trailing-edge vortex is released and becomes a free vortex when $\mathrm{d}\gamma_n/\mathrm{d}t$ changes sign, at which time another tethered vortex is placed at the airfoil trailing edge whose motion and instantaneous circulation are determined by Eq. (7) and Eq. (9), respectively.

Equation (7) can be rearranged into the equivalent scalar form

$$\frac{\mathrm{d}z_{\gamma_n}^*}{\mathrm{d}t} + (H_1 - iH_2)\frac{1}{\gamma_n}\frac{\mathrm{d}\gamma_n}{\mathrm{d}t} = v_{\gamma_n}^*, \tag{10}$$

where $z_{\gamma_n}^* = x - iy$ and $v_{\gamma_n}^* = v_x - iv_y$. The functions H_1 and H_2 involve the stream functions Ψ_j and their derivatives. Equation (10) is the equivalent scalar form of the emended Brown and Michael equation, which is employed for the theoretical analysis in this work. Specific details related to the derivation of Eq. (10) and the expressions of H_1 and H_2 from [16] are presented in the Appendix for reference. Also,

$$v_{\gamma_n}^* = -\frac{i\gamma_n\zeta''(z_{\gamma_n})}{4\pi\zeta'(z_{\gamma_n})} + F'_{\gamma_n}(z_{\gamma_n}), \tag{11}$$

is the complex velocity of the shed vortex with self-potential velocity excluded [13], and the first term on the right side of Eq. (11) is the so-called Routh's correction [17], and the second term is the desingularized complex velocity at z_{γ_n},

$$F'_{\gamma_n}(z_{\gamma_n}) = \zeta' \left[\frac{\mathrm{d}w}{\mathrm{d}\zeta} + \frac{i\gamma_n}{2\pi} \frac{1}{\zeta - \zeta_{\gamma_n}} \right]. \tag{12}$$

D. Kinematics of the incident and free vortices

Similarly, the complex velocity of the incident line vortex at s_Γ is [13]

$$\frac{\mathrm{d}s^*_\Gamma}{\mathrm{d}t} = -\frac{i\Gamma\zeta''(s_\Gamma)}{4\pi\zeta'(s_\Gamma)} + F'(s_\Gamma), \tag{13}$$

where

$$F'_\Gamma(s_\Gamma) = \zeta' \left[\frac{\mathrm{d}w}{\mathrm{d}\zeta} + \frac{i\Gamma}{2\pi} \frac{1}{\zeta - \zeta_\Gamma} \right]. \tag{14}$$

Also, the equation of motion for each of the $n-1$ free vortices is

$$\frac{\mathrm{d}s^*_{\gamma_k}}{\mathrm{d}t} = -\frac{i\gamma_k\zeta''(s_{\gamma_k})}{4\pi\zeta'(s_{\gamma_k})} + F'_{\gamma_k}(s_{\gamma_k}), \tag{15}$$

where

$$F'_{\gamma_k}(s_{\gamma_k}) = \zeta' \left[\frac{\mathrm{d}w}{\mathrm{d}\zeta} + \frac{i\gamma_k}{2\pi} \frac{1}{\zeta - \zeta_{\gamma_k}} \right]. \tag{16}$$

E. Airfoil motion and loads

The airfoil moves aeroelastically under its lift force and the equation of motion of the elastic mount,

$$m\frac{d^2h}{dt^2} + c_d\frac{dh}{dt} + k_h h = -L', \tag{17}$$

where $h(t)$ denotes the vertical displacement of the airfoil (postive downward). The airfoil suspension is modeled as a linear harmonic oscillator with mass m, damping coefficient c_d, and spring stiffness k_h. The unsteady lift force L' is determined by [18]:

$$L' = \rho U\Gamma_a(t) + \rho \int_0^c \frac{\partial}{\partial t}\Gamma_a(x,t)\,\mathrm{d}x\,. \tag{18}$$

III. Results

In this section we first compare the results of a simpler case against Manela's work [19] to validate the mathematical framework, then plot new findings for the aeroelastic case. The model equations are nondimensionalized by $\overline{x} = x/(2\lambda)$, $\overline{y} = y/(2\lambda)$, $\overline{t} = Ut/(2\lambda)$, which produce the following parametric groups that define the numerical simulations [20]:

$$\overline{\Gamma} = \frac{\Gamma}{4\pi U\lambda},\ \overline{\omega}_n = \frac{2\lambda\omega_n}{U},\ \mu = \frac{4\rho_a l_t}{\pi\rho c},\ \xi = \frac{c_d}{2m\omega_n}.$$

The last three parameters are related to the airfoil suspension, where ρ_a is the airfoil density, $\omega_n = \sqrt{k_h/m}$ is the natural frequency of the suspension. The airfoil chord length and λ are related by $c = 3\lambda - 2f_{x0} - \lambda^2/(2f_{x0} - \lambda)$.

A. Comparison with experiments

First, a comparison is made with an experimental study by Peng and Gregory [21] on the interaction of an incident vortex with an NACA0012 airfoil immersed in uniform flows. They investigated the vortex decay during the interaction, and the vortex trajectories with different initial vertical vortex locations. In our current study, we used a symmetric

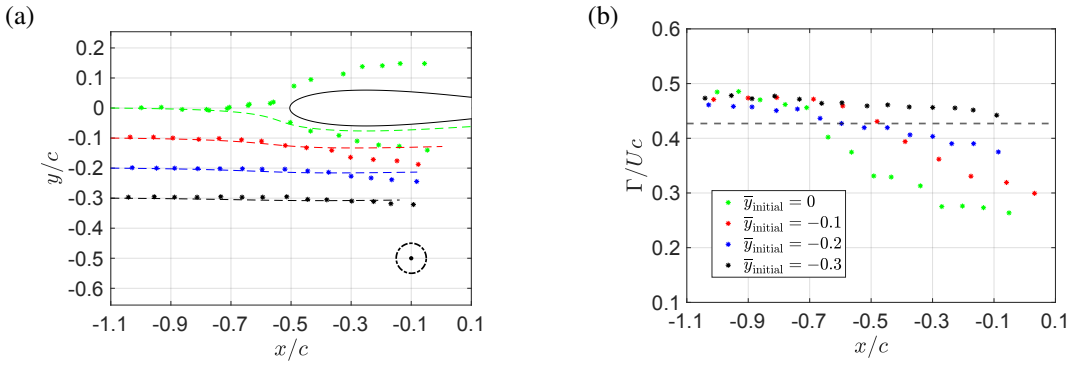

Fig. 3 Comparisons of analytic simulation and experimental measurement [21] on vortex trajectories and strength with different initial vertical locations at 0, -0.1, -0.2 and -0.3. Curves with asterisks are experimental results, dash lines are analytic results. The circle in (a) denotes the size vortex core in the experiment, whose diameter is 0.1c.

Joukowski airfoil with 12% thickness by setting the circle center f_0 to (-0.092, 0). Different dimensionless initial vertical locations are set to be $\bar{y}_{\text{initial}} = \{0, -0.1, -0.2, -0.3\}$. It is worth noting that the decaying of vortex strength is not considered in current analytic work due to inviscid model setup. We choose the same initial vortex strength $\Gamma/(Uc) = -0.427$ (clockwise), c is the chord length of the airfoil. Figure 3 shows the comparison between current inviscid model simulation and experimental measurements. The experimental results are marked in asterisks with different colors for different initial vortex positions, and the associated simulation results are shown in dash lines with different colors. In the experiment, the viscous mechanism becomes dominant when the vortex is enough far from the airfoil, and leads to mild vortex decay due to the shear stress near the surface of the airfoil. Therefore, for the initial vortex locations at -0.2 and -0.3, both blue and black dash lines agree with the experiment results when the vortex is far from the airfoil, and small deviations of the results are observed after the vortex passing by $x/c > -0.3$ which may due to the displacement thickness of the boundary layer. However, for the initial vortex location at -0.1 and 0, large deviations of the vortex trajectories between the current simulation and the experiments when the vortex is in the proximity of the airfoil. From Fig. 16 (b) in Peng and Gregory [21], although a significant loss in vortex strength (30% to 40%) is found due to the deceleration effects of the strong adverse pressure gradient near the leading-edge of the airfoil, the vortex decay may still not explain the large deviations of the results. Need to note that for the initial location at 0, the experiment result shows that the vortex collides with the airfoil leading-edge due to the large radius of vortex core (0.1c), and its trajectory is cut into two separate branches either below or above the airfoil, and such results are not reflected by current simulation result due to a point vortex setup. Thus, our inviscid simulation model may not well predict the experimental measurements when the vortex is near the airfoil due to the complexity of the vortex decay, the vortex boundary layer interaction, the vortex leading-edge interaction, viscous effects, and etc. However, our model shows good agreement with the experimental results when there is enough distance between the vortex and the airfoil.

Another comparison is made between current analytic simulation model and another experimental work by Peng and Gregory [22]. The initial vortex strength is set to be $\Gamma/(Uc) = -0.196$ (clockwise), and vortex decay is also not considered in the analytic simulation. Figure 6 (a) shows the comparisons of vortex trajectories for different initial locations at 0.05 and -0.05, the dash lines denotes the analytic results, and the curve in asterisks are the experimental results. Similar to the results shown in Fig. 3, large deviations of vortex trajectories are observed in Fig. 4(a) when the separation distance between the vortex and the airfoil is small. For the initial location at 0.05, however, the vortex passes above the airfoil in the experimental measurements, while it still passes below the airfoil in the current simulation. Attention is paid to the conditions that makes the vortex pass above the airfoil. First, by fixing the vortex strength, we study the effect of different vortex locations in determining the vortex trajectory. Figure 4(b) shows that the increasing of vortex initial location $\overline{y}_{\text{initial}}$ significantly affects the corresponding vortex trajectories. As the location increases to 0.111, the vortex finally passes above the airfoil and the vortex trajectory offsets downward due to its clockwise direction and its interaction with the airfoil. It is worth mentioning that the effect of vortex strength is also considered in the current study, by fixing the initial location, our simulation result shows that the decreasing of vortex strength cannot make the vortex pass above the airfoil due to the lower initial vortex location.

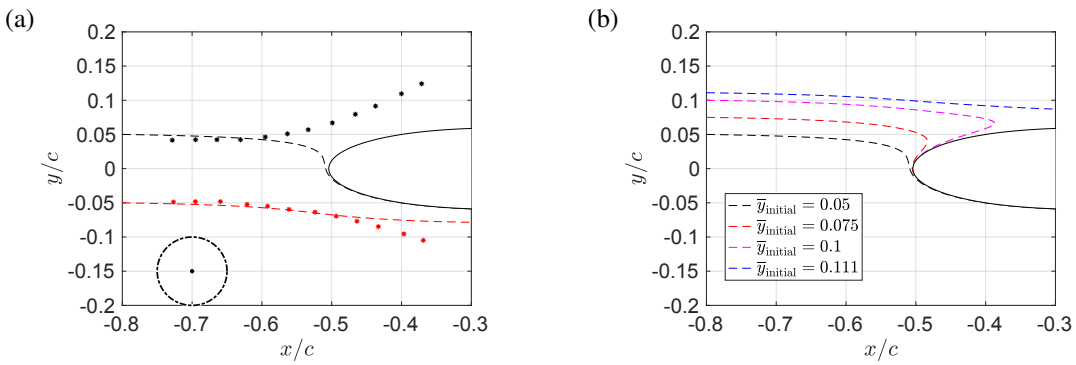

Fig. 4 (a) Comparisons of analytic simulation and experimental measurement [22] on vortex trajectories with different initial vertical locations at 0.05 and -0.05. (b) Vortex paths with different initial vortex locations at 0.05, 0.075, 0.1 and 0.111. Curves with asterisks are experimental results, dash lines are analytic results. The circle in (a) denotes size of the vortex core in the experiment, whose diameter is 0.1c.

B. Aeroelastic case

Attention is now turned to the aeroelastic interactions between the airfoil, the incident, wake and bound vorticity. The conditions to achieve direct vortex impingement on the airfoil are explored with respect to different aerodynamic parameters. The numerical simulations are initialized with initial shed vortex location, $\overline{z}_\gamma(0) = z_\gamma(0)/(2\lambda) = (1, 10^{-6})$, and the initial x-coordinate of the incident vortex is $\Delta\overline{x} = x_0(0)/(2\lambda) = -20$. The mass ratio is fixed to $\mu = 10$, which is representative of an aluminum airfoil with 12% thickness in air. The airfoil thickness is controlled by setting the circle center f_0 in Eq. (2) to (-0.092,0), and the angle of attack is not considered. Structural damping is neglected ($\xi = 0$) in all cases presented in this work.

1. Investigation of vortex impingement

In terms of the initial conditions, the mathematical model is controlled by two dimensionless parameters: the strength of the incident vortex, $\overline{\Gamma}$, and the reduced natural frequency of the oscillator, $\overline{\omega}_n$. Different initial locations of the incident vortex result in the passage of the incident vortex either above or below the airfoil. Here, the bisection method is used to infer the initial vortex position $\Delta\overline{y}$ to achieve direct airfoil impingement given $\overline{\Gamma}$ and $\overline{\omega}_n$. The accuracy of $\Delta\overline{y}$ is controlled by the tolerance of the bisection method, which is set to be $\overline{\varnothing} = \varnothing/(2\lambda) = 0.01$ in the present work. Figure 5 shows the incident vortex trajectories for different initial vortex positions and the corresponding time histories of the airfoil circulation. Figure 5(a) compares the trajectories of the incident vortex in the aeroelastic simulations with different initial locations, including the impingement-occurring location $(\Delta\overline{x}, \Delta\overline{y}) = (-20, -0.31)$ determined by the bisection method, respectively, against the steady streamlines of the flow field in the absence of vortices for visual reference. For the initial location $(20, -0.4)$, the incident vortex follows initially the steady streamline from the left inflow locations and moves below the airfoil at large times. As the initial location moves up to the impingement location $(20, -0.31)$, the incident vortex aligns with the steady streamline at early times. However, near the airfoil, the vortex path deviates backward under influence of the shed vorticity and airfoil motion and moves along a path near the stagnation streamline at the airfoil. As the initial location of the incident vortex moves upward, smaller deviation of the path of the incident vortex is observed in Fig. 5(a).

Figure 5(b) presents the time variations of the airfoil circulation for the shedding of the first two trailing-edge vortices. For the cases when the initial vortex location is $(-20, 0)$ and $(-20, -0.1)$, which causes the incident vortex to move above the airfoil, the corresponding magnitutes of the airfoil circulation time histories increase similarly at early times. These time histories have a sharp change when the incident vortex passes closest to the airfoil due to the shedding of the second vortex. However, for the case when the initial vortex will moves below the airfoil, a small limit and an extended flat response in the airfoil circulation with respect to time can be seen in the dashed line of Fig. 5(b), which may infer a weak interaction between the incident vortex and the airfoil. When the initial vortex location is set to $(-20, -0.31)$, which results in vortex impingement, a similar variation of the airfoil circulation can be observed in the dash-dot line of Fig. 5(b), compared with the solid line and the dotted line. However, the shedding of the second vortex is delayed when the incident vortex passes near the stagnation streamline at the airfoil.

Furthermore, the effects of different aeroelastic parameters such as $\overline{\Gamma}$ and $\overline{\omega}_n$ on the selection of initial incident vortex

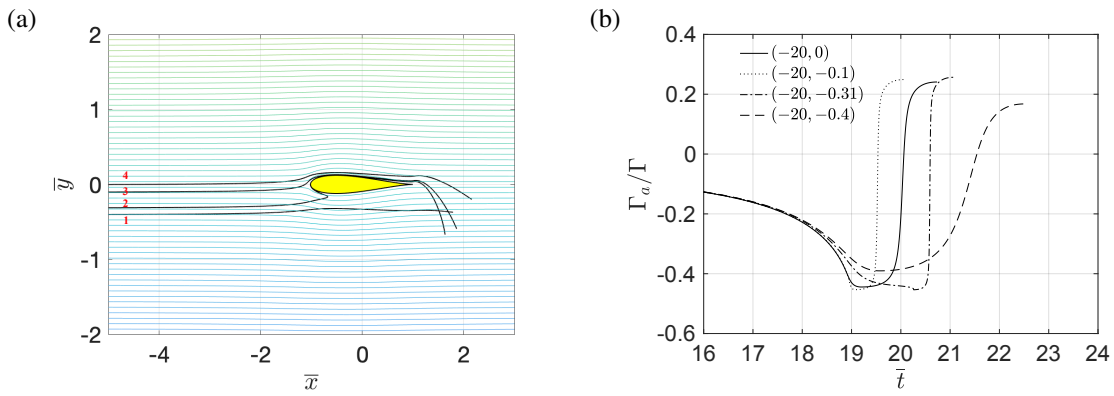

Fig. 5 Time histories of incident vortex trajectories and the bound circulation for different initial vortex positions, with reduced natural frequency $\overline{\omega}_n$ = 0.5, and the strength of the incident vortex $\overline{\Gamma}$ = 0.1: (a) time-varying trajectories of the incident line vortex Γ (denoted 1, 2, 3, 4) resulting from an incident vortex Γ with different initial positions at (-20,-0.4), (-20,-0.31), (-20,-0.1), and (-20,0) past along a symmetrical Joukowski airfoil with 12% thickness. The streamlines in the flow field are for the case where all vortices are absent, and the motion of the indicent vortex across these lines under the influence of the airfoil is noted; (b) time variations of corresponding bound circulation on the airfoil during the shedding of the first two trailing-edge vortices.

locations to achieve vortex impingement are studied. In testing the current numerical scheme, the vortex impingement commonly occurs in the shedding of the first trailing-edge vortex, in which time the downwash effect of the wake may be neglected. The tolerance of the bisection method is set to be $\overline{\varnothing} = \varnothing/(2\lambda) = 0.01$ in the present work. This tolerance produces accurate results, but the solver developed by the authors did not permit smaller tolerance values due to the sensitivity of the numerical scheme to the complexity of aerodynamic model.

Figure 6 (a) presents results for the vortex initial vertical position to achieve direct airfoil impingement as a function for $\overline{\omega}_n$ for $\overline{\Gamma} = 0.1$. In these simulations, the downwash effect of the airfoil wake has been neglected in the aerodynamic model to achieve a reasonable numerical tolerance. It is clear from Fig. 6 (a) that there are upper and lower asymptotic limits on the values of $\Delta\overline{y}$, where $\Delta\overline{y} \to -0.17$ for small values of $\overline{\omega}_n$, and $\Delta\overline{y} \to -0.328$ for large values. Recalling that these simulations are performed at fixed mass ratio, $\mu = 10$, and have no structural damping, $\xi = 0$, the lower and upper limits correspond to negligible spring restoring force (free airfoil) and dominant spring (rigid support) limits. Importantly, the results demonstrate a monotonic change in initial vortex position $\Delta\overline{y}$ with respect to the reduced natural frequency for a given value, and these values of $\Delta\overline{y}$ are bounded by the low and high frequency limits of $\overline{\omega}_n$.

Next consider the case of a fixed reduced natural frequency, $\overline{\omega}_n = 0.5$, where the initial incident vortex locations $\Delta\overline{y}$ can be determined as a function of the incident vortex strength $\overline{\Gamma}$, as shown in Fig. 6 (b). In Fig. 6 (b), the monotonically decreasing value of $\Delta\overline{y}$ with increasing $\overline{\Gamma}$ indicates the need for lower vortex positioning for direct impingement for stronger incident vortices.

Part II

IV. Self-induced rotation of trailing vortices

Self-induced motion arises when vortices are deformed or curved. A kinematical understanding of these structures is important for the trajectory prediction of trailing vortices that result from either prescribed or aeroelastic motions of an aircraft wing. Seminal computational work by Garmann and Visbal [11] into wing encounters with such vortices led to the observation that a these vortex structures rotated as they advected away from the inflow condition towards the wing. This unexpected result motivated a theoretical investigation to determine whether or not the vortex rotation was indeed a fluid dynamical effect or some other effect, such as a numerical error or long-range vortex-wing interaction.

To this end, the work of Bliss [23] on the kinematics of perturbed trailing vortices was revisited and recast into parameters suitable to for modern characterization of the Batchelor trailing vortex and other vortex types. The theoretical analysis assumes a sinusoidal distortion of an infinitely-long vortex, which is different from the computational situation

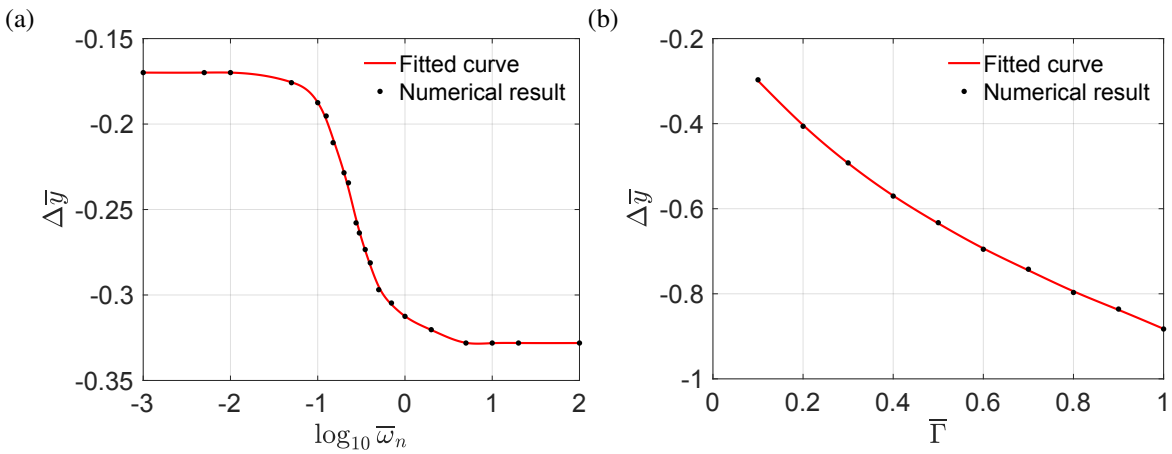

Fig. 6 (a)Effect of reduced natural frequency $\overline{\omega}_n$ on the initial incident vortex vertical position $\Delta\overline{y}$ to achieve direct airfoil impingement. Incident vortex has a strength of $\overline{\Gamma} = 0.1$ and moves past a symmetric Joukowski airfoil with 12% thickness;(b)Variations of selection of initial incident vortex location $\Delta\overline{y}$ with varying strength of incident vortex $\overline{\Gamma}$ when vortex impingement occurs, with reduced natural frequency $\overline{\omega}_n = 0.5$.

of prescribing a vortex plane on the inflow boundary and allowing it to evolve downstream. Nonetheless, the analysis supports the conclusion that the rotation of the vortex structure is due to the self-induced motion, where the direction of vortex rotation is observed and predicted to be in the opposite direction of the rotation of the flow within the vortex core. Preliminary quantitative predictions from theory furnish rough estimates of the vortex rotation observed in [11], which motivates a refinement of the theoretical model to include the effect a variation in the swirl and axial velocity profiles along axis of the vortex.

A. Mathematical model for vortex rotation

Bliss [23] predicts the dynamics of a sinusoidally-perturbed finite-core vortex that is initially straight with axisymmetric (but otherwise arbitrary) swirl and axial velocity radial profiles. The spatial perturbation of the vortex centerline is assumed to be planar, i.e. $a_y \sin kx$, where k is related to the wavelength λ by $k = 2\pi/\lambda$. Widnall *et al.* [24] survey the matched asymptotic procedure of Bliss [23], where the flow solutions internal and external to the vortex core are matched using the ratio of the vortex core radius to the radius of curvature, $\epsilon = r_0/R \ll 1$. Choosing the minimum value of the local curvature of the perturbation, the asymptotic matching parameter may be written as

$$\epsilon = (2\pi)^2 \frac{r_0 a_y}{\lambda^2}. \tag{19}$$

The perturbed vortex executes a rigid body rotation about the unperturbed vortex axis with constant angular velocity (cf. Eq. (6.39) in [23])

$$\Omega_\mathrm{p} = \frac{1}{2}\kappa k^2 \left[\ln\frac{1}{kr_0} + A - C + (\ln 2 - \gamma)\right], \tag{20}$$

where $\kappa = \Gamma/(2\pi)$, Γ is the vortex circulation, γ is Euler's constant, and A and C are constants related to the initial swirl and axial velocity profiles, respectively. Note that the rotation due to Ω_p is in the direction *opposite* to the rotation of fluid inside the vortex core.

The constant A is defined by (cf. Eq. (3.71) in [23])

$$A \equiv I_1(s) - \ln s, \tag{21}$$

where

$$I_1(s) = \int_0^{\bar{r}} \bar{r} v_0^2 \, d\bar{r} \quad \text{for } 0 \le \bar{r} < s. \tag{22}$$

The swirl velocity profile must satisfy the form

$$v_0 = \begin{cases} v_0(\bar{r}) & 0 \le \bar{r} \le s, \\ 1/\bar{r} & s < \bar{r} < \infty, \end{cases} \tag{23}$$

and s is chosen by the asymptotic matching procedure such that $v_0 = 1/\bar{r}$ for $\bar{r} > s$. Similarly, the constant C is defined by (cf. Eq. (3.80) in [23])

$$C \equiv -I_3(s), \tag{24}$$

where

$$\int_0^{\bar{r}} \bar{r}^2 \frac{d(w_0^2)}{d\bar{r}}\, d\bar{r} = \begin{cases} I_3(s) & 0 \le \bar{r} \le s, \\ -C & s < \bar{r} < \infty, \end{cases} \tag{25}$$

and

$$w_0 = \begin{cases} w_0(\bar{r}) & 0 \le \bar{r} \le s, \\ 0 & s < \bar{r} < \infty. \end{cases} \tag{26}$$

It must be emphasized that, despite the form of Eqs. (21) and (24), A and C are constants and do not depend on s.

For a Batchelor vortex [25] with a decaying vortex core, Eqs. (4.32) and (4.48) in [23] provide the following nondimensional swirl and axial velocity profiles,

$$v_0 = \frac{1}{\bar{r}}\left[1 - e^{-\bar{r}^2}\right], \tag{27}$$

$$w_0 = \alpha\, e^{-\bar{r}^2}, \tag{28}$$

where the velocities have been rescaled by κ/r_0 [24] and α is a specified nondimensional value. Bliss [23] shows that these velocity distributions lead to

$$A = \frac{\gamma}{2} - \frac{1}{2}\ln 2 \approx -0.058, \tag{29}$$

$$C = \frac{\alpha^2}{2} \tag{30}$$

Note that C is positive semi-definite, i.e. the effect of the axial velocity profile on the vortex motion does not depend on whether or not there is an axial velocity excess or deficit.

We now recast the results of Bliss [23] in terms of the vortex parameters relevant to the computational study carried out by Garmann and Visbal [11]. In their formulation, the dimensional swirl and axial velocity profiles of the vortex imposed on the inflow boundary condition are

$$v_0 = \frac{\Gamma}{2\pi r}\left[1 - e^{-(r/r_0)^2}\right], \tag{31}$$

$$w_0 = \Delta u\, e^{-(r/r_0)^2}, \tag{32}$$

again noting that the sign of Δu is irrelevant on the vortex rotation within the context of the theoretical model, cf. Eq. (30). The relationship between the swirl and axial velocities is the swirl parameter q defined by

$$q = \frac{\Gamma}{2\pi r_0 \Delta u} = \frac{\kappa}{r_0 \Delta u}. \tag{33}$$

Now nondimensionalizing the velocities in Eqs. (31) and (32) by κ/r_0 in the same manner as Bliss [23] and letting $\bar{r} = r/r_0$,

$$v_0 = \frac{1}{\bar{r}}\left[1 - e^{-\bar{r}^2}\right], \tag{34}$$

$$w_0 = \frac{1}{q}\, e^{-\bar{r}^2}, \tag{35}$$

where we recover the same swirl velocity profile as Eq. (27) and identify $\alpha = 1/q$.

The rotation rate of the vortex (20) may now be expressed as

$$\Omega_\mathrm{p} = 2\pi^2 q \frac{\Delta u\, r_0}{\lambda^2}\left[\ln\frac{\lambda}{2\pi r_0} - \frac{1}{2}q^{-2} + \frac{1}{2}(\ln 2 - \gamma)\right]. \tag{36}$$

Note that the rotation rate of the vortex structure does not depend on the amplitude of the sinusoidal perturbation a_y; however, this value remains important in establishing the range of validity for the theoretical model per Eq. (19).

Let us now presume that the vortex structure advects with a uniform background flow U such that its change in location may be written as $\Delta x = Ut$, and the change in angular displacement of the vortex can be expressed by $\theta_\mathrm{p} = \Omega_\mathrm{p} t = \Omega_\mathrm{p} \Delta x / U$.

$$\theta_\mathrm{p} = 2\pi^2 q \frac{\Delta u}{U} \frac{\Delta x\, r_0}{\lambda^2} \left[\ln \frac{\lambda}{2\pi r_0} - \frac{1}{2} q^{-2} + \frac{1}{2} (\ln 2 - \gamma) \right]. \tag{37}$$

B. Comparison with computational results

Garmann and Visbal [11] use the following parameters to define their trailing vortex, where the lengths are referenced to an airfoil chord length c.

$$\begin{aligned} q &= 2.0 \\ \Delta u &= 0.4U \\ r_0 &= 0.1c \\ \lambda &= 5c \\ a_y &= 0.25c,\ 0.5c \end{aligned}$$

These values furnish the result

$$\theta_\mathrm{p} = 0.1268 \frac{\Delta x}{c} = 7.26^\circ \frac{\Delta x}{c}, \tag{38}$$

where the amount of vortex rotation at locations $\Delta x/c = 5$ and 9.5 are $\theta_\mathrm{p} = 36.3^\circ$ and 69.0°, respectively. We underscore that these results are based upon an assumption that the vortex centerline continues to remain planar as the vortex structure rotates about the axis of the originally undeformed (and axially uniform) vortex; the vortex in [11] continues to evolve downstream of the inflow condition and is not strictly periodic in the streamwise direction. For the parameters in [11], the logarithm term in Eq. (37) dominates the terms in the square brackets. Also, it should be noted that the values of the asymptotic matching parameter are $\epsilon = 0.039$ and 0.079 for $a_y = 0.25c$ and $0.5c$, respectively. The theoretical predictions for θ_p are independent of the amplitude of the vortex deformation, a_y.

In Fig 7 of [11], the sinusoidal, linear motion of the vortex at the inflow persists downstream as the entire vortex structure rotates, particularly for the small-amplitude case where $a_y = 0.25c$. For this case at $\Delta x/c = 5$ and 9.5, $\theta_\mathrm{p} \approx 16^\circ$ and 47°, which are less than predicted by the Bliss theory. However, θ_p increases faster than a linear function of the streamwise distance, indicating that the differences between the physical scenarios of the theory and computation, as well as perhaps the evolution of the swirl and axial velocity profiles in the computation, impact the rotation of the vortex structure.

V. Conclusions

Part I of this paper simulates the aeroelastic interactions of an incident line vortex with a symmetric Joukowski airfoil of 12% thickness on an elastic suspension. The mathematical framework is modelled by using dynamic conformal mapping techniques. The dynamical problem for the incident vortex motion and trailing edge wake evolution is studied using the potential flow theory and the Brown and Michael equation, and thin airfoil theory is applied to analyze the aeroelastic motion of the airfoil with the vortical field.

Results from the mathematical framework are compared against recent experimental study by Peng and Gregory [21], where the present simulations match well with the experiments when the vortex is far from the airfoil with mild decay of strength. However, the inviscid model developed in this work may not be used to simulate the vortex motions near the airfoil due to multiple aspects of influence, such as viscous vortex–boundary-layer interaction, vortex decay, or viscous vortex–leading-edge interaction. An additional comparison of the inviscid numerical model with the experimental campaign of Peng and Gregory [22] studies the effects of different vortex strength and initial locations on the vortex trajectories. The present simulation results show similar vortex trajectories to the experiments by increasing the initial vortex locations, while decreasing the vortex strength may not help with the vortex trajectory.

Apart from these comparisons for vortex interactions with fixed airfoils, the present work also extends consideration to the aeroelastic case, in which the conditions to achieve direct impingement of an incident line vortex with the elastically-mounted airfoil are explored. The aeroelastic results of a symmetric Joukowski airfoil with 12% thickness

demonstrate that the incident vortex follows initially the steady streamline in the uniform flow, but deviates backward and then moves along a path near the stagnation streamline at the airfoil near where the vortex impingement occurs. The numerical results also indicate a weak sensitivity of the vortex initial vertical position to the reduced natural frequency of the airfoil elastic suspension when this frequency is either small or large, but the initial vortex placement for airfoil impingement changes monotonically with the natural frequency in a specific range that depends on the vortex strength.

The work in Part I is an extension and combination of previous efforts in other work by Chen and Jaworski [10, 16, 20] involving similar gust-airfoil interaction problem with different model setups. The present framework can be extended to consider the vortex-airfoil response in air or water. The extension of this work may involve a corresponding acoustic analysis in the future.

Part II develops a simple predictive model for the self-induced rotation of a streamwise-oriented vortex with a planar, sinusoidal deformation along its axis. The small-deformation theory of Bliss [23] yields angular displacements of the vortex that are larger by more than a factor of two when compared against numerical simulations of undulating Batchelor vortices. The source of this analytical and numerical discrepancy is the subject of ongoing research and may be related to differences in configuration as well as the evolution of the vortex core and its influence on vortex kinematics that are not accounted for in Bliss's theory.

Appendix

Scalar form of emended Brown and Michael equation

The original emended Brown and Michael equation is [12]

$$\frac{\mathrm{d}\boldsymbol{x}_{\gamma_n}}{\mathrm{d}t}\cdot\boldsymbol{\nabla}\Psi_i+\frac{\Psi_i}{\gamma_n}\frac{\mathrm{d}\gamma_n}{\mathrm{d}t}=\boldsymbol{v}_{\gamma_n}\cdot\boldsymbol{\nabla}\Psi_i,\qquad i=1,2. \tag{39}$$

Equation (39) can be expanded in vector formats as

$$\left(\frac{\mathrm{d}x}{\mathrm{d}t},\frac{\mathrm{d}y}{\mathrm{d}t}\right)\cdot\left(\frac{\partial\Psi_1}{\partial x},\frac{\partial\Psi_1}{\partial y}\right)+\frac{\Psi_1}{\gamma_n}\frac{\mathrm{d}\gamma_n}{\mathrm{d}t}=\left(v_x,v_y\right)\cdot\left(\frac{\partial\Psi_1}{\partial x},\frac{\partial\Psi_1}{\partial y}\right), \tag{40}$$

$$\left(\frac{\mathrm{d}x}{\mathrm{d}t},\frac{\mathrm{d}y}{\mathrm{d}t}\right)\cdot\left(\frac{\partial\Psi_2}{\partial x},\frac{\partial\Psi_2}{\partial y}\right)+\frac{\Psi_2}{\gamma_n}\frac{\mathrm{d}\gamma_n}{\mathrm{d}t}=\left(v_x,v_y\right)\cdot\left(\frac{\partial\Psi_2}{\partial x},\frac{\partial\Psi_2}{\partial y}\right). \tag{41}$$

Equations (40) and (41) can be also expanded respectively as

$$\frac{\mathrm{d}x}{\mathrm{d}t}\frac{\partial\Psi_1}{\partial x}+\frac{\mathrm{d}y}{\mathrm{d}t}\frac{\partial\Psi_1}{\partial y}+\frac{\Psi_1}{\gamma_n}\frac{\mathrm{d}\gamma_n}{\mathrm{d}t}=v_x\frac{\partial\Psi_1}{\partial x}+v_y\frac{\partial\Psi_1}{\partial y}, \tag{42}$$

$$\frac{\mathrm{d}x}{\mathrm{d}t}\frac{\partial\Psi_2}{\partial x}+\frac{\mathrm{d}y}{\mathrm{d}t}\frac{\partial\Psi_2}{\partial y}+\frac{\Psi_2}{\gamma_n}\frac{\mathrm{d}\gamma_n}{\mathrm{d}t}=v_x\frac{\partial\Psi_2}{\partial x}+v_y\frac{\partial\Psi_2}{\partial y}. \tag{43}$$

From (42) and (43), the general scalar form of emended Brown and Michael equation may be written as

$$\frac{\mathrm{d}x}{\mathrm{d}t}+\frac{\Psi_1\frac{\partial\Psi_2}{\partial y}-\Psi_2\frac{\partial\Psi_1}{\partial y}}{\frac{\partial\Psi_1}{\partial x}\frac{\partial\Psi_2}{\partial y}-\frac{\partial\Psi_2}{\partial x}\frac{\partial\Psi_1}{\partial y}}\frac{1}{\gamma_n}\frac{\mathrm{d}\gamma_n}{\mathrm{d}t}=v_x, \tag{44}$$

$$\frac{\mathrm{d}y}{\mathrm{d}t}+\frac{\Psi_1\frac{\partial\Psi_2}{\partial x}-\Psi_2\frac{\partial\Psi_1}{\partial x}}{\frac{\partial\Psi_1}{\partial y}\frac{\partial\Psi_2}{\partial x}-\frac{\partial\Psi_2}{\partial y}\frac{\partial\Psi_1}{\partial x}}\frac{1}{\gamma_n}\frac{\mathrm{d}\gamma_n}{\mathrm{d}t}=v_y. \tag{45}$$

Let

$$H_1=\frac{\Psi_1\frac{\partial\Psi_2}{\partial y}-\Psi_2\frac{\partial\Psi_1}{\partial y}}{\frac{\partial\Psi_1}{\partial x}\frac{\partial\Psi_2}{\partial y}-\frac{\partial\Psi_2}{\partial x}\frac{\partial\Psi_1}{\partial y}}, \tag{46}$$

$$H_2=\frac{\Psi_1\frac{\partial\Psi_2}{\partial x}-\Psi_2\frac{\partial\Psi_1}{\partial x}}{\frac{\partial\Psi_1}{\partial y}\frac{\partial\Psi_2}{\partial x}-\frac{\partial\Psi_2}{\partial y}\frac{\partial\Psi_1}{\partial x}}. \tag{47}$$

Expressions (44) and (45) can be rearranged into

$$\frac{\mathrm{d}z^*_{\gamma_n}}{\mathrm{d}t} + (H_1 - iH_2)\frac{1}{\gamma_n}\frac{\mathrm{d}\gamma_n}{\mathrm{d}t} = v^*_{\gamma_n}, \tag{48}$$

where $z^*_{\gamma_n} = x - iy$, and $v^*_{\gamma_n} = v_x - iv_y$.

Equation (48) can be regarded as a general scalar form of the emended Brown and Michael equation for future theoretical analyses. Once the stream function Ψ_i $(i = 1, 2)$ is known, it is possible to get $\boldsymbol{\nabla}\Psi_i = (\,\partial\Psi_i/\partial x\,,\,\partial\Psi_i/\partial y\,)$, thus H_1 and H_2 are known, and the vortex motion can be analyzed from Eq. (48).

Acknowledgments

This work was supported in part by the Air Force Office of Scientific Research under AFOSR grants FA9550-15-1-0148 and FA9550-19-1-0095, monitored by Drs. Douglas Smith and Gregg Abate, and by the National Science Foundation under awards 1805692 and 1846852, monitored by Dr. Ronald Joslin. Preliminary results from this paper appeared previously as parts of AIAA Paper 2018-2907 at 2018 Fluid Dynamics Conference [16] and AIAA Paper 2019-0897 at the 2019 AIAA SciTech Forum [20].

References

[1] Rockwell, D. O., "Vortex-body interactions," *Annual Review of Fluid Mechanics*, Vol. 30, 1998, pp. 199–229.

[2] Howe, M., "Elastic blade-vortex interaction noise," *Journal of Sound and Vibration*, Vol. 177, No. 3, 1994, pp. 325–336.

[3] Manela, A., "Sound generated by a vortex convected past an elastic sheet," *Journal of Sound and Vibration*, Vol. 330, No. 3, 2011, pp. 416–430.

[4] Manela, A., "Nonlinear effects of flow unsteadiness on the acoustic radiation of a heaving airfoil," *Journal of Sound and Vibration*, Vol. 332, No. 26, 2013, pp. 7076–7088.

[5] Rockwell, D., and Knisely, C., "The organized nature of flow impingement upon a corner," *Journal of Fluid Mechanics*, Vol. 93, No. 3, 1979, pp. 413–432.

[6] Ziada, S., and Rockwell, D., "Vortex–leading-edge interaction," *Journal of Fluid Mechanics*, Vol. 118, 1982, pp. 79–107.

[7] Conlisk, A., and Rockwell, D., "Modeling of vortex-corner interaction using point vortices," *The Physics of Fluids*, Vol. 24, No. 12, 1981, pp. 2133–2142.

[8] Conlisk, A., and Veley, D., "The generation of noise in impinging vortex motion past a step," *The Physics of Fluids*, Vol. 28, No. 10, 1985, pp. 3004–3012.

[9] Panaras, A. G., "Numerical modeling of the vortex/airfoil interaction," *AIAA Journal*, Vol. 25, No. 1, 1987, pp. 5–11.

[10] Chen, H., "Vortex gust interactions with oscillating Joukowski airfoil," Master's thesis, Lehigh University, May 2018.

[11] Garmann, D. J., and Visbal, M. R., "Unsteady interactions of a wandering streamwise-oriented vortex with a wing," 32nd *AIAA Applied Aerodynamics Conference, Atlanta, GA*, Paper AIAA-2014-2105, 2014.

[12] Howe, M. S., "Emendation of the Brown & Michael equation, with application to sound generation by vortex motion near a half-plane," *Journal of Fluid Mechanics*, Vol. 329, 1996, pp. 89–101.

[13] Howe, M. S., *Theory of vortex sound*, Vol. 33, Cambridge University Press, United Kingdom, 2003.

[14] Batchelor, G. K., *An introduction to fluid dynamics*, Cambridge University Press, United Kingdom, 1967.

[15] Howe, M. S., *Acoustics and aerodynamic sound*, Cambridge University Press, United Kingdom, 2014.

[16] Chen, H., and Jaworski, J. W., "Vortex interactions with Joukowski airfoil on elastic supports," *AIAA Fluid Dynamics Conference, Atlanta, GA*, Paper AIAA-2018-2907, 2018.

[17] Clements, R., "An inviscid model of two-dimensional vortex shedding," *Journal of Fluid Mechanics*, Vol. 57, No. 2, 1973, pp. 321–336.

[18] Katz, J., and Plotkin, A., *Low-speed aerodynamics*, 2nd ed., Cambridge University Press, United Kingdom, 2001.

[19] Manela, A., and Huang, L., "Point vortex model for prediction of sound generated by a wing with flap interacting with a passing vortex," *The Journal of the Acoustical Society of America*, Vol. 133, No. 4, 2013, pp. 1934–1944.

[20] Chen, H., and Jaworski, J. W., "Aeroelastic trajectory selection of vortex gusts impinging upon Joukowski airfoils," *2019 AIAA SciTech Forum*, 2019, p. 0897.

[21] Peng, D., and Gregory, J. W., "Vortex dynamics during blade-vortex interactions," *Physics of Fluids*, Vol. 27, No. 5, 2015, p. 053104.

[22] Peng, D., and Gregory, J. W., "Asymmetric distributions in pressure/load fluctuation levels during blade-vortex interactions," *Journal of Fluids and Structures*, Vol. 68, 2017, pp. 58–71.

[23] Bliss, D. B., "The dynamics of curved rotational vortex lines," Master's thesis, Massachusetts Institute of Technology, 1970.

[24] Widnall, S. E., Bliss, D., and Zalay, A., "Theoretical and experimental study of the stability of a vortex pair," *Aircraft Wake Turbulence and Its Detection*, edited by J. Olsen, A. Goldberg, and M. Rogers, Plenum, New York, 1971, pp. 305–338.

[25] Batchelor, G. K., "Axial flow in trailing line vortices," *Journal of Fluid Mechanics*, Vol. 20, No. 4, 1964, pp. 645–658.